iScience

CellPress

Article

Sodium Ion Capacitor Using Pseudocapacitive Layered Ferric Vanadate Nanosheets Cathode

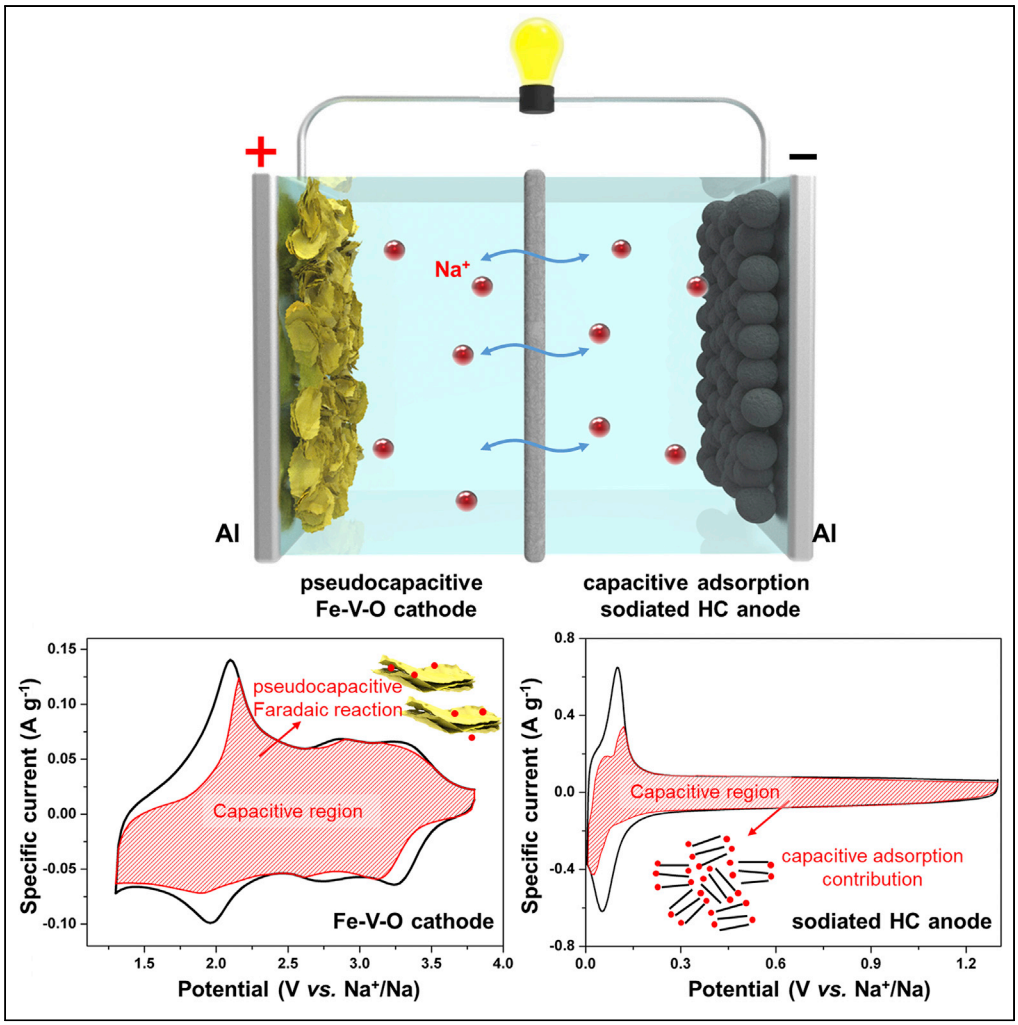

Qiulong Wei, Yalong Jiang, Xiaoshi Qian, ..., Qinyou An, Jinghua Guo, Liqiang Mai

anqinyou86@whut.edu.cn (Q.A.)
mlq518@whut.edu.cn (L.M.)

HIGHLIGHTS

Pseudocapacitive cathode is applied to construct a high-energy sodium ion capacitor

Layered ferric vanadate cathode displays pseudocapacitive sodium storage behavior

Ferric vanadate cathode delivers remarkable rate capability and cycling stability

Hard carbon anode exhibits capacitive adsorption mechanism and high-rate performance

Wei et al., iScience 6, 212–221
August 31, 2018
https://doi.org/10.1016/j.isci.2018.07.020

iScience

CellPress

Article

Sodium Ion Capacitor Using Pseudocapacitive Layered Ferric Vanadate Nanosheets Cathode

Qiulong Wei,[1,2] Yalong Jiang,[1] Xiaoshi Qian,[2] Liang Zhang,[3] Qidong Li,[1] Shuangshuang Tan,[1] Kangning Zhao,[1] Wei Yang,[1] Qinyou An,[1,*] Jinghua Guo,[3] and Liqiang Mai[1,4,*]

SUMMARY

Sodium ion capacitors (SICs) are designed to deliver both high energy and power densities at low cost. Electric double-layer capacitive cathodes are typically used in these devices, but they lead to very limited capacity. Herein, we apply a pseudocapacitive layered ferric vanadate (Fe-V-O) as cathode to construct non-aqueous SICs with both high energy and power densities. The Fe-V-O nanosheets cathode displays remarkable rate capability and cycling stability. The pseudocapacitive sodium storage mechanism of Fe-V-O, with over 83% of total capacity from capacitive contribution, is confirmed by kinetics analysis and *ex situ* characterizations. The capacitive-adsorption mechanism of hard carbon (HC) anode is demonstrated, and it delivers excellent rate capability. Based on as-synthesized materials, the assembled HC//Fe-V-O SIC delivers a maximum energy density of 194 Wh kg^{-1} and power density of 3,942 W kg^{-1}. Our work highlights the advantages of pseudocapacitive cathodes for achieving both high energy and power densities in sodium storage devices.

INTRODUCTION

Electrochemical energy storage (EES) devices play an indispensable role in our daily life owing to their widespread applications in portable electronics, electric vehicles, and large-scale regenerative energy storage systems (Lukatskaya et al., 2016; Wei et al., 2017a). Among these, Li-ion batteries (LIBs) offer high energy density (150–200 Wh kg^{-1}) but not enough power density (<1 kW kg^{-1}) (Lukatskaya et al., 2016; Wang et al., 2017a). The electrostatic double-layer capacitance (EDLC) can offer transitory high power output (>1 kW kg^{-1}), but the low energy density (<10 Wh kg^{-1}) limits their further applications (Wang et al., 2017a; Zuo et al., 2017). The goal of next-generation EES devices is to achieve high energy density close to that of LIBs and high power density close to that of EDLCs (Lukatskaya et al., 2016; Zuo et al., 2017). In this case, a method of combining the operation mechanism of both LIBs and EDLCs to simultaneously utilize their individual advantages for the charge storage processes is proposed, that is, the first-generation hybrid ion capacitors (HICs) (Aravindan et al., 2014). Since 2001, Amatucci and co-workers (Amatucci et al., 2001) constructed a hybrid Li^+-ion capacitor (LIC) by using an EDLC-type activated carbon (AC) cathode and a nanostructured battery-type $Li_4Ti_5O_{12}$ anode, which delivered an energy density up to 20 Wh kg^{-1} (~3 times that of a conventional carbon-based supercapacitor). After that, many HICs were developed, such as Nb_2O_5//AC (Deng et al., 2018a), MoS_2//AC (Cook et al., 2017), Li_3VO_4//AC (Shen et al., 2017), and so forth (Wang et al., 2017a; Zuo et al., 2017). The energy densities of HICs were gradually improved (approached 140 Wh kg^{-1}), which show great promising applications.

The market of lithium-relate EES devices is huge and is rapidly growing; unfortunately, the lithium resource is limited (Deng et al., 2018b). As an emerging technology that could complement current LIBs/LICs, sodium ion storage technology has attracted much attention due to the low cost and wide distribution of abundant sodium resource (Deng et al., 2018b; Luo et al., 2016; Ni et al., 2018; Ren et al., 2017). Having similar configurations as LICs, the general sodium ion capacitors (SICs) are using the AC as cathode and the battery-type or pseudocapacitive oxides/sulfides as anode (Dong et al., 2017; Wang et al., 2017a). Recently, many investigations on the SICs have been published, indicating the wide attention in this area. Several SIC configurations, such as $NaTi_2(PO_4)_3$//AC (Wei et al., 2017a, 2017b), Nb_2O_5//AC (Deng et al., 2018a; Lim et al., 2016), TiO_2//AC (Le et al., 2017), Ti(O,N)//AC (Dong et al., 2017), and $Na_2Ti_3O_7$//AC (Dong et al., 2016), show advantages in high-rate applications. Till now, most of these concepts have used the high surface area of EDLC-type AC as the cathode. The EDLCs utilize non-faradaic electrostatic

[1]State Key Laboratory of Advanced Technology for Materials Synthesis and Processing, International School of Materials Science and Engineering, Wuhan University of Technology, Wuhan 430070, China

[2]Department of Materials Science and Engineering, University of California Los Angeles, Los Angeles, CA 90095, USA

[3]Advanced Light Source, Lawrence Berkeley National Laboratory, Berkeley, CA 94720, USA

[4]Lead Contact

*Correspondence: anqinyou86@whut.edu.cn (Q.A.), mlq518@whut.edu.cn (L.M.)

https://doi.org/10.1016/j.isci.2018.07.020

ion adsorption at the surface or inside pores to store charge, and the storage capacity is very limited (Augustyn et al., 2014a). The battery-type $Na_2Fe_2(SO_4)_3$ cathode has been used for SIC with enhanced capacity and energy; however, its unstratified reaction kinetics when matched with high pseudocapacitive Ti_2C-MXene anode hindered the rate performance of the full capacitor (Wang et al., 2015). High-capacity cathode materials with excellent rate performance are relatively less explored, but much more are expected. The pseudocapacitance arises when reversible faradaic redox reaction at or near the surface of a material in contact with electrolyte, which delivers much higher capacitance than EDLCs but still with high rate capability (Augustyn et al., 2014a, 2014b; Lukatskaya et al., 2016). In this case, an appropriate pseudocapacitive cathode instead of an EDLC-type AC with much enlarged capacity is urgently required. Therefore, much higher energy density, close to battery level, will be expected. However, till date, this kind of cathode, especially for sodium storage, remains largely unexploited.

Layered transition metal oxides (TMOs) with two-dimensional channels for Na^+ ion intercalation are the most promising sodium storage materials (Deng et al., 2018b; Han et al., 2015; Yabuuchi et al., 2014). Recently, different phases and nano-morphologies of TMOs have shown attractive sodium storage performance (Dall'Agnese et al., 2015; Fang et al., 2017; Guo et al., 2017; Hwang et al., 2017; Raju et al., 2014; Su and Wang, 2013; Wang et al., 2017b). However, they rarely demonstrate pseudocapacitive storage abilities, especially for the ones used as cathodes. Wei et al. reported that the $V_2O_5 \cdot nH_2O$ xerogel with large interlayer spacing (~11.53 Å) delivered a high capacity up to 338 mAh g^{-1} and an impressive pseudocapacitive sodium storage behavior (Wei et al., 2015a). However, the layered vanadium oxide xerogel structure was unstable during long-term cycles. The vanadates, derivatives of vanadium-based materials, with increased electronic conductivity and enlarged/stabilized layer structure without blocking ion diffusion show promising electrochemical performance (Durham et al., 2016). Sodium vanadate ($Na_{1.25}V_3O_8$ and $Na_{1.1}V_3O_{7.9}$) showed excellent cyclability and rate capability as a sodium storage cathode (Dong et al., 2015; Yuan et al., 2015). Among the families of vanadates, ferric vanadates are abundant and natural. The Kazakhstanite phase [$Fe_5V_{15}O_{39}(OH)_9 \cdot 9H_2O$, known as Fe-V-O], one of the ferric vanadates, has a large layered spacing (d_{002} = 10.51 Å), which is beneficial for sodium diffusion. However, the detailed charge storage mechanism and reaction kinetics are unclear yet.

For anode materials, hard carbon (HC) is regarded as the most promising material (Li et al., 2018; Hou et al., 2017; Yabuuchi et al., 2014). HC has a "house-of-cards" structure, containing graphite-like microcrystallites and amorphous carbon. Liu and co-workers recently confirmed the "adsorption-intercalation" sodium storage process in HC materials (Qiu et al., 2017). In detail, the Na^+ ions first absorb on the active sites on the HC surface, leading to a sloping voltage profile (above 0.2 V versus Na^+/Na). Then, Na^+ ions intercalate into the graphite-like microcrystallites, showing a flat voltage plateau (below 0.2 V versus Na^+/Na). The electrochemical performance and the contribution of capacity from the adsorption and intercalation regions are related to the microstructure (Hou et al., 2017; Qiu et al., 2017). In this work, we utilize the capacitive adsorption mechanism of HC anode and match it with the high-rate pseudocapacitive cathode to assemble an SIC with both high energy and high power densities.

Herein, the sodium storage performance of the layered Fe-V-O nanosheets (NSs) cathode is investigated, which delivers a high reversible sodium storage capacity up to 229 mAh g^{-1} at 0.25 C (1C = 200 mA g^{-1}), excellent rate capability, and cycling stability. The pseudocapacitive sodium storage mechanism is further demonstrated by *ex situ* characterizations and detailed electrochemical kinetics analysis. Furthermore, we assemble an SIC, utilizing the high pseudocapacitive Fe-V-O cathode and capacitive adsorption HC anode (Hou et al., 2017; Qiu et al., 2017), which shows remarkable electrochemical performance. Owing to the pseudocapacitive Fe-V-O cathode having much higher capacity than that of AC, the assembled HC//Fe-V-O SIC delivers a high energy density of ~194 Wh kg^{-1}, which is very close to battery level. Meanwhile, the SIC shows excellent high average power density up to 3,942 W kg^{-1} with a high energy density of 32 Wh kg^{-1}. This work demonstrates that pseudocapacitive cathodes are promising candidates for the next-generation SICs with both high energy and power density.

RESULTS

Structure and Morphology Characterization of Fe-V-O NSs

Figure 1A shows the X-ray diffraction (XRD) patterns of the as-synthesized Fe-V-O sample. All the peaks are indexed to a pure phase of $Fe_5V_{15}O_{39}(OH)_9 \cdot 9H_2O$ (monoclinic, a = 11.84 Å, b = 3.65 Å, c = 21.27 Å, β = 100°, JCPDS Card No. 46-1334) (Poizot et al., 2003; Wei et al., 2018). Fourier transform infrared spectrum

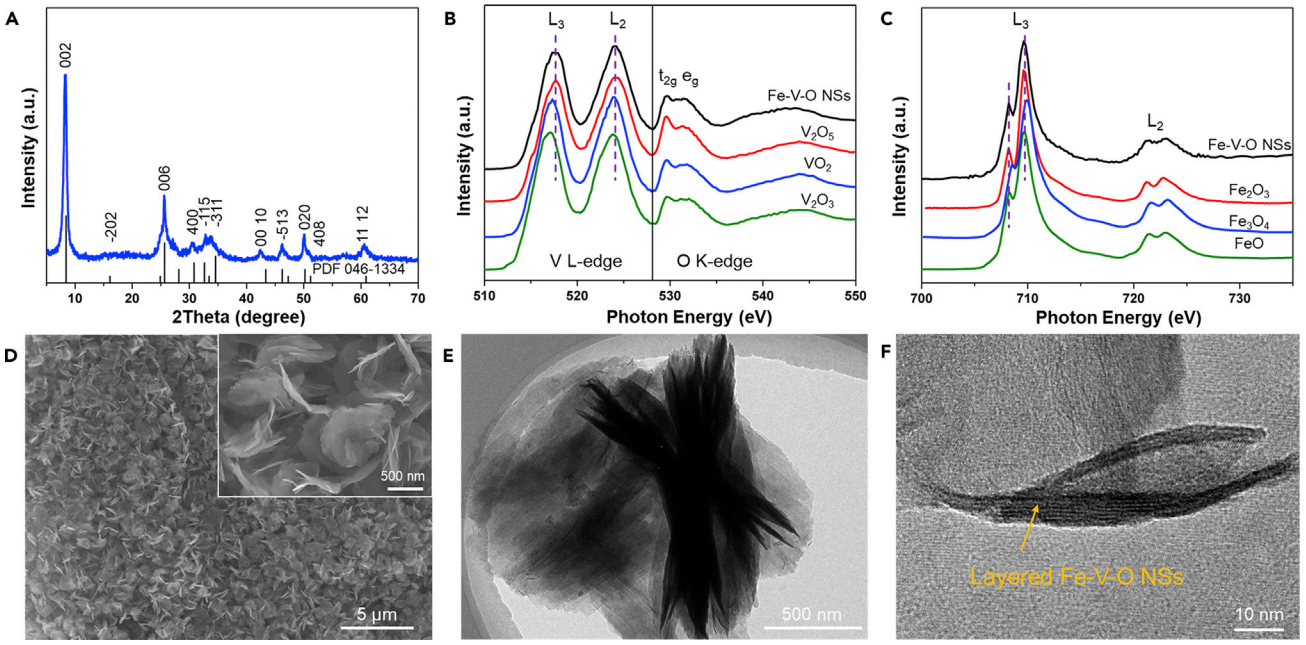

Figure 1. Phase and Morphology Characterization of Layered Fe-V-O NSs

(A) XRD patterns of the layered Fe-V-O NSs. XAS L-edge spectra of V (B) and Fe (C). Scanning electron micrograph (D) and TEM (E) and high-resolution TEM (HRTEM) (F) images of layered Fe-V-O NSs.

See also Figures S1–S3.

(Figure S1) shows the stretching vibration of O–H band (3,400 cm^{-1}) and the symmetric band of δ(H_2O) vibrations (1,624 cm^{-1}), indicating the existence of water molecules (Wei et al., 2015a, 2015b). The peaks at 537 cm^{-1} (out-of-plane V-O-V vibrations) and 1,004 cm^{-1} (V=O stretching bond) are the characteristics of vanadium oxide layered structure (Wei et al., 2015a, 2015b). The electronic states of vanadium and iron for Fe-V-O NSs were further investigated by X-ray absorption spectroscopy (XAS) and X-ray photoelectron spectroscopy (XPS). The V L-edge XAS spectra (Figure 1B) demonstrate two sets of features located at the ranges of 513–520 eV and 520–528 eV, respectively, corresponding to the L_3-edge and L_2-edge. The V L-edge spectrum of Fe-V-O resembles the convolution of the spectra of VO_2 and V_2O_5, indicating that the valence state of vanadium in Fe-V-O NSs is between +5 and +4. Detailed V 2p XPS spectrum analysis (Figure S2A and Table S1) reveals that the content of V^{5+} is much higher than that of V^{4+} for Fe-V-O and the ratio of V^{5+} to V^{4+} is ~13.8:1.2 (Wei et al., 2015a). In addition, the spectral shape and peak position of the Fe L-edge XAS spectrum (Figure 1C) of Fe-V-O NSs is similar to that of Fe_2O_3, indicating the existence of Fe^{3+}, which is consistent with the Fe 2p XPS-fitting results (Figure S2B).

The morphology and detailed microstructure of the as-synthesized sample were investigated using scanning electron microscopy (SEM) and transmission electron microscopy (TEM). The panoramic view of the sample (Figures 1D and 1E) reveals a uniform large-scale nanosheet morphology with an average size of ~1 μm, indicating a high yield of the facile synthesis method. Specifically, the two-dimensional NSs nanostructures are very attractive for electrode materials owing to the high surface area exposed to the electrolyte, short ion/electron diffusion distance, and facile strain relaxation (Anasori et al., 2017; Augustyn et al., 2014b). The large layered fringes observed at the edge of nanosheets indicate the layered structure of the Fe-V-O (Figure 1F). The energy-dispersive X-ray spectroscopy result (Figure S3) reveals an atomic ratio of V:Fe of ~3.23:1. The Brunauer-Emmet-Teller (BET) specific surface area of NSs is 34 $m^2\ g^{-1}$.

Sodium Storage Performance of Fe-V-O NSs Cathode

The electrochemical performance of Fe-V-O NSs was investigated by assembling half-cells (2025-type coin cell) with sodium as anode. Galvanostatic test at 0.25 C (50 mA g^{-1}) in a potential range of 1.3–3.8 V (versus Na^+/Na) was first performed. The charge-discharge curves of the Fe-V-O NSs cathode (Figure 2A) displays slope line curves. The initial discharge capacity of Fe-V-O cathode is 229.8 mAh g^{-1}, indicating a charge

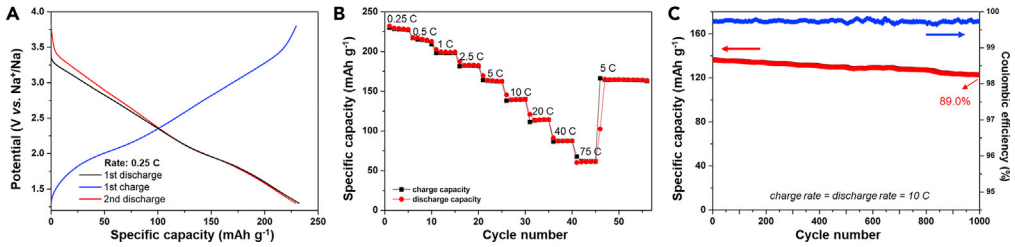

Figure 2. Sodium Storage Performance of Layered Fe-V-O NSs Cathode

(A) Charge-discharge curves of the layered NSs at a rate of 0.25 C in 1.3–3.8 V. Rate performance (B) and long-term cycling performance at 10 C (C) of layered Fe-V-O NSs cathode.

See also Figure S4.

storage of ~17 mol Na^+ per unit formula. The calculation is based on the equation: $n = (3.6MC)/F$, where n is the ion storage number, F is the Faraday constant, C is he capacity, and M is the molecular weight. The subsequent charge and discharge capacity is 229.5 and 229.3 mAh g^{-1}, respectively, indicating highly reversible sodiation/desodiation process.

The rate performance at progressively increased rates (ranging from 0.25 to 75 C) was further measured (Figure 2B). A high capacity of 199, 164, 139, and 114 mAh g^{-1} at 1, 5, 10, and 20 C are obtained, respectively. Even at higher rates of 40 and 75 C, the Fe-V-O NSs cathode delivers a high capacity of 87 and 61 mAh g^{-1}, respectively. Figure S4 shows the charge-discharge curves from the rate testing. The slope lines are observed at various rates and the overpotential is very small, indicating the fast reaction kinetics (Xu et al., 2018). Owing to rapid changes of current density, the electrode exhibits very stable capacity at each current. When the current is turned back to 5 C, almost 100% of the capacity is recovered and there is no obvious capacity loss after the following 10 cycles. The Fe-V-O NSs cathode also shows remarkable long-term cycling performance (Figure 2C), that is, a capacity retention of 89% after 1,000 cycles at a high rate of 10 C. The rate capability of layered Fe-V-O NSs is better than those reported for state-of-the-art vanadium oxide and vanadate cathodes (Dong et al., 2015; Liu et al., 2017; Nam et al., 2015; Raju et al., 2014; Su and Wang, 2013; Wei et al., 2015a; Yuan et al., 2015).

Sodium Storage Mechanism and Kinetics Analysis of Fe-V-O NSs Cathode

Ex situ XRD of the Fe-V-O cathodes at different discharged and charged states were measured to investigate the structural changes during sodiation/desodiation processes. As shown in Figure 3A, the (002) diffraction peak shifts to higher angles (interlayer spacing distance is reduced) after sodiation, owing to the enhanced coordination reaction between the layers by the intercalation of Na^+ ions (Wei et al., 2015a). During the sodiation and desodiation process, the (002) diffraction peaks shift almost negligibly (d_{002} is stable at ~8.97 Å), indicating no phase change (as a characteristic for the typical pseudocapacitive behavior) (Augustyn et al., 2014a). After one cycle, the layer spacing of Fe-V-O keeps the electrochemical activated state, which inhibits layer breathings during the following Na^+ intercalation/extraction (Wang et al., 2015; Wei et al., 2015a). The very small layered lattice breathing is good for obtaining excellent cyclability (Augustyn et al., 2013; Le et al., 2017).

The *ex situ* XPS spectra of Fe-V-O cathode after discharge to 1.3 V (Figures 3B and 3C) were further collected to investigate the valence changes of vanadium and iron during sodiation reaction. After peak fitting, it is clearly seen that both vanadium (Figure 3B) and iron (Figure 3C) are reduced. Based on the calculation of valence changes from XPS data (Table S1), the average valence state of vanadium is reduced from +4.92 to +3.90, indicating that the total transferred charge from the redox of vanadium is 15.32 mol e^- per unit formula. Iron valence is reduced from +3.00 to +2.66, according to 1.02 mol e^- per unit formula, from the redox of iron. Charge storage is mainly from the redox of vanadium rather than that of iron. The total redox reaction (16.34 mol e^- per unit formula) obtained from the XPS analyses was very closed to the delivered capacity (~17 mol Na^+ per unit formula), confirming the faradaic redox charge storage mechanism of Fe-V-O NSs cathode.

Kinetics analysis was further undertaken based on cyclic voltammetry (CV) method. The CV curves of Fe-V-O NSs cathode at various scan rates are shown in Figure 3D. A couple of redox peaks located at

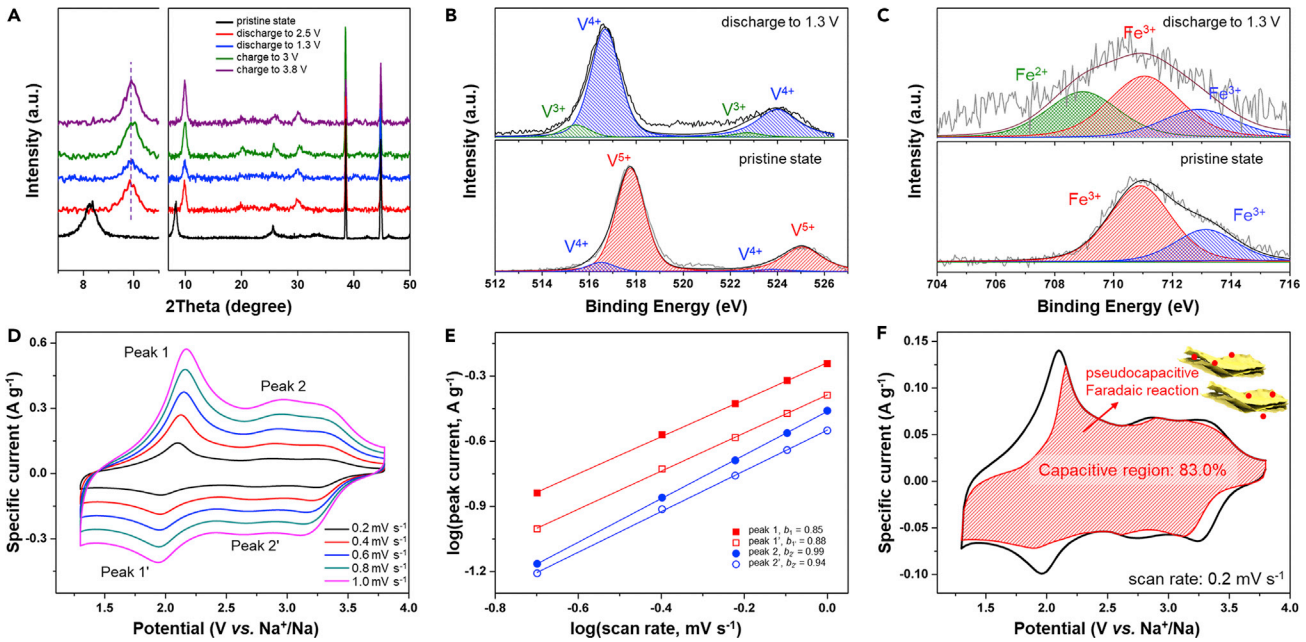

Figure 3. Pseudocapacitive Sodium Storage Mechanism of Layered Fe-V-O NSs Cathode

(A) *Ex situ* XRD patterns of Fe-V-O NSs cathodes at various discharged and charged states.

(B and C) *Ex situ* V 2p (B) and Fe 2p (C) XPS spectra of the Fe-V-O NSs cathode at pristine state and discharged to 1.3 V. The redox reaction obtained from the XPS analyses confirms the pseudocapacitive charge storage mechanism.

(D) CV curves of layered Fe-V-O NSs at various scan rates from 0.2 to 1.0 mV s^{-1}.

(E) The peak currents versus scan rates plots to determine the *b*-value of the anodic and cathodic peaks.

(F) Capacitive contributions (shaded area) to charge storage at a scan rate of 0.2 mV s^{-1}.

See also Table S1.

~2.10 and 1.96 V (versus Na^+/Na) and a rectangular shape are observed. The redox peaks shift slightly with the increasing scan rates, indicating excellent reaction kinetics (Augustyn et al., 2013). A related analysis is taken to investigate the relationship between peak current (*i*) and scan rate, according to Equation 1 (Augustyn et al., 2013; Wang et al., 2017a).

$$i = a\nu^b \qquad \text{(Equation 1)}$$

The value of $b = 0.5$ indicates semi-infinite linear diffusion controlled charge storage, whereas $b = 1$ means capacitive-dominated charge storage (Augustyn et al., 2013). The *b*-value can be obtained by plotting log(*i*) versus log(*v*) (Figure 3E). After linear fitting, the *b*-values of peaks 1/1′ and 2/2′ are 0.85/0.88 and 0.99/0.94, respectively. The *b*-values are very closed to 1, indicating a capacitive-dominated process.

Further calculation of the diffusion and capacitive contributions to the total capacity are done by using Equation (2), in which the current (*i*) at a potential (V) comes from capacitive- ($k_1\nu$) and diffusion-controlled contributions ($k_2\nu^{1/2}$) (Wei et al., 2017a; Zuo et al., 2017).

$$i(V) = k_1\nu + k_2\nu^{1/2} \qquad \text{(Equation 2)}$$

The capacitive contribution is analyzed to be at a rate of 0.2 mVs^{-1}, whereas the capacity contribution from the diffusion process is maximization at relatively slow rate. The shaded region (Figure 3F) shows the obvious capacitive contribution area of Fe-V-O NSs cathode, whereas the calculated percentage is 83.0%. Based on the above XPS analysis, it is proved that the capacitive behavior is dominated by faradaic pseudocapacitive ratio rather than that of EDLC. From the total capacity (792 C g^{-1}) obtained by CV performed at 0.2 mV s^{-1} in the range 1.3–3.8 V and taking the capacitive contribution of 83% into account, the capacitance of Fe-V-O obtained is ~262 F g^{-1}. Thus, the normalized specific areal capacitance of Fe-V-O NSs is 771 μF cm^{-2}, which is much higher than that of EDLC (10–20 μF cm^{-2}) (Lukatskaya et al., 2016). This computation demonstrates the pseudocapacitive-dominated sodium storage process, which contributes to delivering fast charge storage.

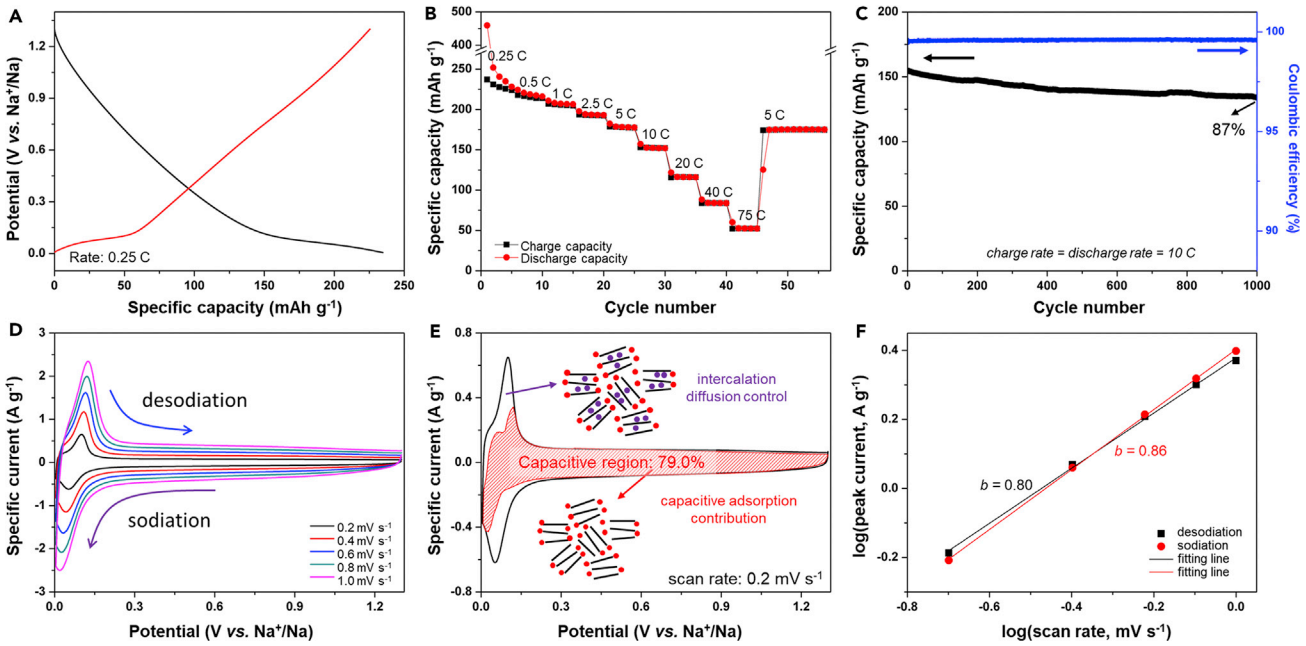

Figure 4. Sodium Storage Performance and Kinetics Analysis of HC Anode

(A–C) (A) Galvanostatic charge-discharge curves of HC anode at 0.25 C in a potential window of 0.001–1.3 V. Rate performance (B) and long-term cycling performance at 10 C (C) of HC anode.

(D) CV curves of HC anode at various scan rates from 0.2 to 1.0 mV s^{-1}.

(E) Capacitive contributions (shaded area) to charge storage at a scan rate of 0.2 mV s^{-1}.

(F) The peak currents versus scan rates plots to determine the *b*-value of the sodiation and desodiation peaks.

See also Figures S5–S7.

Electrochemical Performance and Sodium Storage Mechanism of Hard Carbon Anode

The detailed synthesis and characterizations of HC anode are discussed in the supporting information (Figure S5). The d_{002} of HC is calculated to be 3.80 Å based on the XRD pattern (Figure S5A), which is beneficial for large-sized Na^+ ion insertion (Jian et al., 2016). Raman spectrum (Figure S5B) shows that I_D/I_G is 1.01, indicating the coexistence of graphite layer and disorder region. Figure S5C shows the slope of the N_2 adsorption-desorption isotherms, indicating the existence of nanoporous structure in HC. The BET surface area of HC is ~190 m^2 g^{-1}.

The charge-discharge curves of the HC anode at 0.25 C (50 mA g^{-1}) display the typical sloping voltage and flat plateau regions, consistent with previously reported results (Figure S6) (Saurel et al., 2018). To match the potential range of Fe-V-O cathode, the following cycles of HC anode were tested in the window of 0.001–1.3 V (versus Na^+/Na), as shown in Figure 4A. The initial discharge capacity of HC anode is 459 mAh g^{-1}, whereas subsequently it is 240 mAh g^{-1}, indicating a columbic efficiency (CE) of 52.3%. The low initial CE is due to the reduction of electrolyte and the formation of solid-electrolyte interface (SEI) layers under the low potential (Chen et al., 2015; Jian et al., 2016; Qiu et al., 2017). The rate performance of the HC anode is shown in Figure 4B. The HC anode shows excellent rate capability: a high capacity of 206, 152, and 116 mAh g^{-1} is obtained at the rate of 1, 10, and 20 C, respectively. Even at 40 and 75 C, a high value of 84 and 52 mAh g^{-1} is delivered, respectively. The charge-discharge curves of HC anode (Figure S7) show that the flat plateaus coming from Na^+ ion intercalation/extraction fade away with increasing rate. The cycling performance of HC anode is excellent: a capacity retention of 87% after 1,000 cycles at a rate of 10 C (Figure 4C).

Detailed kinetics analysis of HC anode was investigated further. The CV curves of HC anode at scan rates ranging from 0.2 to 1 mV s^{-1} (Figure 4D) were collected, which show a rectangular shape and a couple of peaks at ~0.10 and 0.05 V, according to the adsorption-intercalation mechanism of HC. Furthermore, the capacitive and diffusion-controlled contributions were distinguished based on Equation 2. The shared region shows the capacitive contribution of 79.0% (Figure 4E), which covers the whole area between 0.2 and

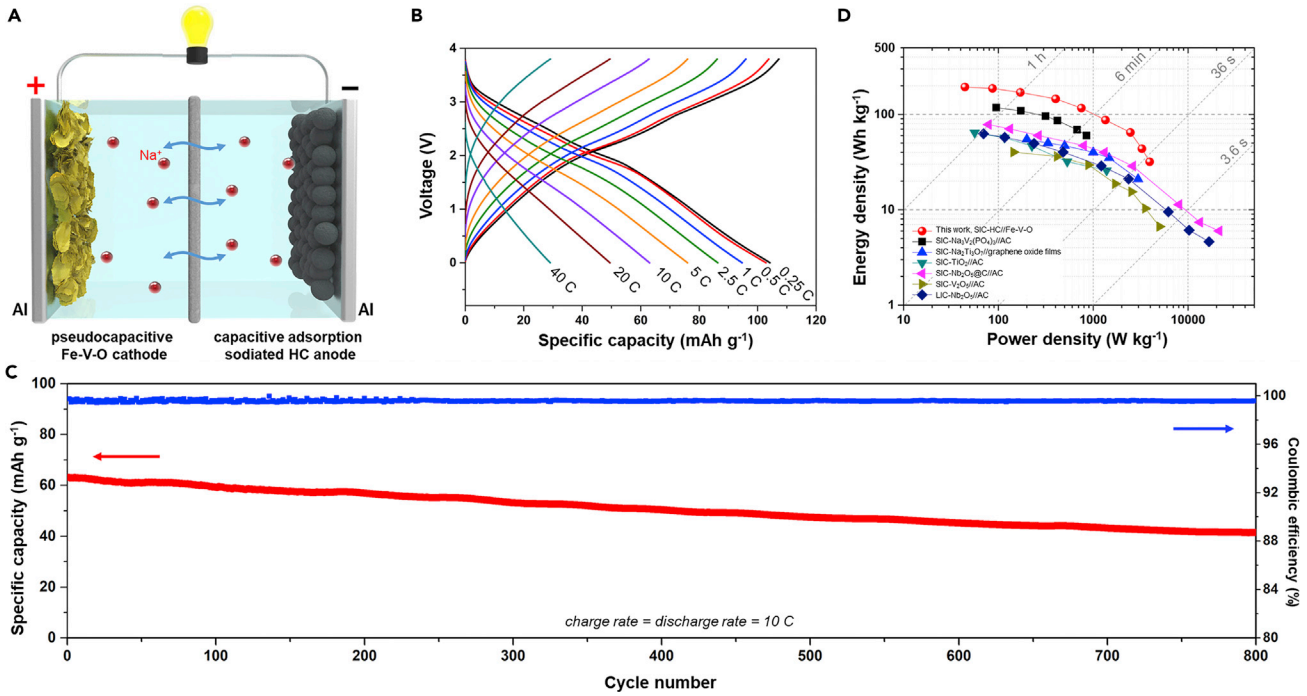

Figure 5. Electrochemical Performance of HC//FeVO Full Sodium Ion Capacitor

(A) Schematic of the SIC, consisting of pseudocapacitive Fe-V-O NSs cathode and capacitive adsorption sodiated HC anode.

(B) The charge-discharge curves of SIC at various rates from 0.25 to 40 C in a voltage window of 0–3.8 V.

(C) Long-term cycling performance of SIC at a rate of 10 C.

(D) Ragone plots of HC//FeVO SIC and the comparisons among other reported SICs: $Na_3V_2(PO_4)_3$//AC (Thangavel et al., 2016), $Na_2Ti_3O_7$//graphene oxide films (Dong et al., 2016), TiO_2//AC (Le et al., 2017), Nb_2O_5@C//AC (Lim et al., 2016), V_2O_5//AC (Chen et al., 2012), and LIC: Nb_2O_5//AC (Lim et al., 2015). See also Figures S8 and S9.

1.3 V and some in the peak location. The absorption of Na^+ ions on the edges/defects of carbon contributes to the capacitive responses in the region. Meanwhile, owing to the size of graphite-like microcrystallites in HC being very small, the diffusion distance of the Na^+ into these layers is very short, leading to some capacitive responses as well (Hou et al., 2017; Qiu et al., 2017). Furthermore, according to Equation 1, the *b* values of sodiated/desodiated peaks are 0.8 and 0.86 (Figure 4F), respectively, consistent with the above discussion. This electrochemical capacitive adsorption behavior is due to the Na^+ ions (1.02 Å) diffusing into the amorphous region and adsorbing on the edges/defects of carbons (Chmiola et al., 2006; Forse et al., 2016). This kind of Na^+ storage behavior is different from the EDLC process (Saurel et al., 2018). Further study on this is worth conducting.

Electrochemical Performance of HC//Fe-V-O NSs Sodium Ion Capacitor

Prompted by the above results, it is expected that the pseudocapacitive Fe-V-O NSs cathode and the capacitive adsorption HC anode are promising candidates for full SIC (Figure 5A). To reduce the irreversibility effect of anode in the initial discharge process and provide the shuttle of Na^+ ions between the cathode and anode, pre-sodiated HC at 0.25 C for 5 cycles was prepared (Le et al., 2017; Li et al., 2016). According to the charge balance, the mass ratio of HC to Fe-V-O is fixed as 1:1. The Fe-V-O cathodes deliver very similar rate performance in the half-cell (Figure 2B) and the full SIC tests (Figure S8), owing to the well-matched storage kinetics between the cathode and anode (Figure S9) (Wang et al., 2017a). The full SIC shows slope charge and discharge curves in a voltage window of 0–3.8 V (Figure 5B). The capacity and energy density of SIC are calculated based on the mass of cathode and sodiated anode materials. The discharge capacity of the full SIC is 104 mAh g^{-1} at 0.25 C. The SIC delivers effective cycles at different rates from 0.25 to 40 C. The capacity is 103, 95, 74, and 60 mAh g^{-1} at 0.5, 1, 5, and 10 C, respectively. Even at high rates of 20 and 40 C, the discharge capacity remains at 49 and 28 mAh g^{-1}, respectively. Figure 5C shows the cycling performance and corresponding coulombic efficiency of the SIC at 10 C. The SIC shows stable

cyclability over 800 cycles with a capacity retention of ~67.2% and coulombic efficiency above 99.5%, indicating the outstanding reversibility of the HC//Fe-V-O full SIC.

The Ragone plots of full SIC (energy density versus power density) are displayed in Figure 5D. The assembled SIC delivers a maximum energy density of ~194 Wh kg^{-1} at an average power density of 45 W kg^{-1}. The maximum energy of SIC reaches that of sodium ion batteries (SIBs) (Deng et al., 2018b; Ren et al., 2017). Meanwhile, the assembled SIC delivers excellent high power density with high energy density. Even at the high average power densities of 750 and 3,942 W kg^{-1}, it shows a high energy density of ~117 and 32 Wh kg^{-1}, respectively. It is instructive to compare the electrochemical performance of HC//Fe-V-O SIC in this work to those of other reported SICs and even LICs. As shown in Figure 5D, HC//Fe-V-O SIC delivers higher energy densities than state-of-the-art SICs (Chen et al., 2012; Dong et al., 2016; Le et al., 2017; Lim et al., 2016; Thangavel et al., 2016) and LICs (Lim et al., 2015). These results show that the as-assembled HC//Fe-V-O SIC is one of the promising energy storage devices with both high energy and power.

DISCUSSION

In summary, the layered Fe-V-O NSs cathode exhibits remarkable pseudocapacitance for sodium storage in non-aqueous system. The capacitive response contributes to over 83% of the total stored charge, which enables ultrahigh rate capability. Making a step forward in the field of full device systems, our asymmetric HC//Fe-V-O SIC shows excellent reversible rate capability and cycling stability. A maximum energy density of 194 Wh kg^{-1} is achieved, close to battery level. Meanwhile, the SIC delivers remarkable high average power density of 3,942 W kg^{-1} with a high energy density of 32 Wh kg^{-1}. Our work highlights the significant advantages of capacitive electrodes for realizing high-rate sodium storage performance. The asymmetric SIC by utilizing the pseudocapacitive cathode and anode delivers remarkable high energy as well as high power performance.

METHODS

All methods can be found in the accompanying Transparent Methods supplemental file.

SUPPLEMENTAL INFORMATION

Supplemental Information includes Transparent Methods, nine figures, and one table and can be found with this article online at https://doi.org/10.1016/j.isci.2018.07.020.

ACKNOWLEDGMENTS

This work was supported by the National Natural Science Fund for Distinguished Young Scholars (51425204), the National Natural Science Foundation of China (51521001, 51602239), the National Key Research and Development Program of China (2016YFA0202603), the Program of Introducing Talents of Discipline to Universities (B17034), the Yellow Crane Talent (Science & Technology) Program of Wuhan City, and the Fundamental Research Funds for the Central Universities (WUT: 2017III005, 2017III009). The work at Advanced Light Source of the Lawrence Berkeley National Laboratory was supported by the Director, Office of Science, Office of Basic Energy Sciences of the U.S. Department of Energy under Contract (DE-AC02-05CH11231).

AUTHOR CONTRIBUTIONS

Q.W. and L.M. conceived the study and co-wrote the manuscript. Q.W., Y.J., L.Z., Q.L., and S.T. carried out the synthesis and electrochemical evaluation. X.Q., L.Z., K.Z., W.Y., J.G., and Q.A. helped with material characterization and manuscript preparation. All authors discussed the results and commented on the manuscript.

DECLARATION OF INTERESTS

The authors declare no competing interests.

Received: March 1, 2018
Revised: July 9, 2018
Accepted: July 23, 2018
Published: August 31, 2018

REFERENCES

Amatucci, G.G., Badway, F., Du Pasquier, A., and Zheng, T. (2001). An asymmetric hybrid nonaqueous energy storage cell. J. Electrochem. Soc. *148*, A930–A939.

Anasori, B., Lukatskaya, M.R., and Gogotsi, Y. (2017). 2D metal carbides and nitrides (MXenes) for energy storage. Nat. Rev. Mater. *2*, 16098.

Aravindan, V., Gnanaraj, J., Lee, Y.-S., and Madhavi, S. (2014). Insertion-type electrodes for nonaqueous Li-ion capacitors. Chem. Rev. *114*, 11619–11635.

Augustyn, V., Come, J., Lowe, M.A., Kim, J.W., Taberna, P.-L., Tolbert, S.H., Abruña, H.D., Simon, P., and Dunn, B. (2013). High-rate electrochemical energy storage through Li^+ intercalation pseudocapacitance. Nat. Mater. *12*, 518.

Augustyn, V., Simon, P., and Dunn, B. (2014a). Pseudocapacitive oxide materials for high-rate electrochemical energy storage. Energy Environ. Sci. *7*, 1597–1614.

Augustyn, V., White, E.R., Ko, J., Grüner, G., Regan, B.C., and Dunn, B. (2014b). Lithium-ion storage properties of titanium oxide nanosheets. Mater. Horiz. *1*, 219–223.

Chen, Z., Augustyn, V., Jia, X., Xiao, Q., Dunn, B., and Lu, Y. (2012). High-performance sodium-ion pseudocapacitors based on hierarchically porous nanowire composites. ACS Nano *6*, 4319–4327.

Chen, C., Wen, Y., Hu, X., Ji, X., Yan, M., Mai, L., Hu, P., Shan, B., and Huang, Y. (2015). Na^+ intercalation pseudocapacitance in graphene-coupled titanium oxide enabling ultra-fast sodium storage and long-term cycling. Nat. Commun. *6*, 6929.

Chmiola, J., Yushin, G., Gogotsi, Y., Portet, C., Simon, P., and Taberna, P.-L. (2006). Anomalous increase in carbon capacitance at pore sizes less than 1 nanometer. Science *313*, 1760–1763.

Cook, J.B., Kim, H.S., Lin, T.C., Lai, C.H., Dunn, B., and Tolbert, S.H. (2017). Pseudocapacitive charge storage in thick composite MoS_2 nanocrystal-based electrodes. Adv. Energy Mater. *7*, 1601283.

Dall'Agnese, Y., Taberna, P.-L., Gogotsi, Y., and Simon, P. (2015). Two-dimensional vanadium carbide (MXene) as positive electrode for sodium-ion capacitors. J. Phys. Chem. Lett. *6*, 2305–2309.

Deng, B., Lei, T., Zhu, W., Xiao, L., and Liu, J. (2018a). In-plane assembled orthorhombic Nb_2O_5 nanorod films with high-rate Li^+ intercalation for high-performance flexible Li-ion capacitors. Adv. Funct. Mater. *28*, 1704330.

Deng, J., Luo, W.B., Chou, S.L., Liu, H.K., and Dou, S.X. (2018b). Sodium-ion batteries: from academic research to practical commercialization. Adv. Energy Mater. *8*, 1701428.

Dong, Y., Li, S., Zhao, K., Han, C., Chen, W., Wang, B., Wang, L., Xu, B., Wei, Q., and Zhang, L. (2015). Hierarchical zigzag $Na_{1.25}V_3O_8$ nanowires with topotactically encoded superior performance for sodium-ion battery cathodes. Energy Environ. Sci. *8*, 1267–1275.

Dong, S., Shen, L., Li, H., Pang, G., Dou, H., and Zhang, X. (2016). Flexible sodium-ion pseudocapacitors based on 3D $Na_2Ti_3O_7$ nanosheet arrays/carbon textiles anodes. Adv. Funct. Mater. *26*, 3703–3710.

Dong, J., Jiang, Y., Li, Q., Wei, Q., Yang, W., Tan, S., Xu, X., An, Q., and Mai, L. (2017). Pseudocapacitive titanium oxynitride mesoporous nanowires with iso-oriented nanocrystals for ultrahigh-rate sodium ion hybrid capacitors. J. Mater. Chem. A *5*, 10827–10835.

Durham, J.L., Poyraz, A.S., Takeuchi, E.S., Marschilok, A.C., and Takeuchi, K.J. (2016). Impact of multifunctional bimetallic materials on lithium battery electrochemistry. Acc. Chem. Res. *49*, 1864–1872.

Fang, Y., Yu, X.Y., and Lou, X.W.D. (2017). A practical high-energy cathode for sodium-ion batteries based on uniform P2-$Na_{0.7}CoO_2$ microspheres. Angew. Chem. Int. Ed. *56*, 5801–5805.

Forse, A.C., Merlet, C.l., Griffin, J.M., and Grey, C.P. (2016). New perspectives on the charging mechanisms of supercapacitors. J. Am. Chem. Soc. *138*, 5731–5744.

Guo, S., Li, Q., Liu, P., Chen, M., and Zhou, H. (2017). Environmentally stable interface of layered oxide cathodes for sodium-ion batteries. Nat. Commun. *8*, 135.

Han, M.H., Gonzalo, E., Singh, G., and Rojo, T. (2015). A comprehensive review of sodium layered oxides: powerful cathodes for Na-ion batteries. Energy Environ. Sci. *8*, 81–102.

Hou, H., Qiu, X., Wei, W., Zhang, Y., and Ji, X. (2017). Carbon anode materials for advanced sodium-ion batteries. Adv. Energy Mater. *6*, 1602898.

Hwang, J.Y., Myung, S.T., and Sun, Y.K. (2017). Sodium-ion batteries: present and future. Chem. Soc. Rev. *46*, 3529–3614.

Jian, Z., Xing, Z., Bommier, C., Li, Z., and Ji, X. (2016). Hard carbon microspheres: potassium-ion anode versus sodium-ion anode. Adv. Energy Mater. *6*, 1602898.

Le, Z., Liu, F., Nie, P., Li, X., Liu, X., Bian, Z., Chen, G., Wu, H.B., and Lu, Y. (2017). Pseudocapacitive sodium storage in mesoporous single-crystal-like TiO_2-graphene nanocomposite enables high-performance sodium-ion capacitors. ACS Nano *11*, 2952–2960.

Li, H., Zhu, Y., Dong, S., Shen, L., Chen, Z., Zhang, X., and Yu, G. (2016). Self-assembled Nb_2O_5 nanosheets for high energy–high power sodium ion capacitors. Chem. Mater. *28*, 5753–5760.

Li, Y., Yuan, Y., Bai, Y., Liu, Y., Wang, Z., Li, L., Wu, F., Amine, K., Wu, C., and Lu, J. (2018). Insights into the Na^+ storage mechanism of phosphorus-functionalized hard carbon as ultrahigh capacity anodes. Adv. Energy Mater. *8*, 1702781.

Lim, E., Jo, C., Kim, H., Kim, M.-H., Mun, Y., Chun, J., Ye, Y., Hwang, J., Ha, K.-S., and Roh, K.C. (2015). Facile synthesis of Nb_2O_5@carbon core–shell nanocrystals with controlled crystalline structure for high-power anodes in hybrid supercapacitors. ACS Nano *9*, 7497–7505.

Lim, E., Jo, C., Kim, M.S., Kim, M.H., Chun, J., Kim, H., Park, J., Roh, K.C., Kang, K., and Yoon, S. (2016). High-performance sodium-ion hybrid supercapacitor based on Nb_2O_5@carbon core–shell nanoparticles and reduced graphene oxide nanocomposites. Adv. Funct. Mater. *26*, 3711–3719.

Liu, J., Chen, Z., Chen, S., Zhang, B., Wang, J., Wang, H., Tian, B., Chen, M., Fan, X., and Huang, Y. (2017). "Electron/ion sponge"-like V-based polyoxometalate: toward high-performance cathode for rechargeable sodium ion batteries. ACS Nano *11*, 6911–6920.

Lukatskaya, M.R., Dunn, B., and Gogotsi, Y. (2016). Multidimensional materials and device architectures for future hybrid energy storage. Nat. Commun. *7*, 12647.

Luo, W., Shen, F., Bommier, C., Zhu, H., Ji, X., and Hu, L. (2016). Na-ion battery anodes: materials and electrochemistry. Acc. Chem. Res. *49*, 231–240.

Nam, K.W., Kim, S., Yang, E., Jung, Y., Levi, E., Aurbach, D., and Choi, J.W. (2015). Critical role of crystal water for a layered cathode material in sodium ion batteries. Chem. Mater. *27*, 3721–3725.

Ni, J., Li, L., and Lu, J. (2018). Phosphorus: an anode of choice for sodium-ion batteries. ACS Energy Lett. *3*, 1137–1144.

Poizot, P., Laruelle, S., Touboul, M., and Tarascon, J.-M. (2003). Wet-chemical synthesis of various iron (III) vanadates (V) by co-precipitation route. C. R. Chim. *6*, 125–134.

Qiu, S., Xiao, L., Sushko, M.L., Han, K.S., Shao, Y., Yan, M., Liang, X., Mai, L., Feng, J., Cao, Y., et al. (2017). Manipulating adsorption-insertion mechanisms in nanostructured carbon materials for high-efficiency sodium ion storage. Adv. Energy Mater. *7*, 1700403.

Raju, V., Rains, J., Gates, C., Luo, W., Wang, X., Stickle, W.F., Stucky, G.D., and Ji, X. (2014). Superior cathode of sodium-ion batteries: orthorhombic V_2O_5 nanoparticles generated in nanoporous carbon by ambient hydrolysis deposition. Nano Lett. *14*, 4119–4124.

Ren, W., Zhu, Z., An, Q., and Mai, L. (2017). Emerging prototype sodium-ion full cells with nanostructured electrode materials. Small *13*, 1604181.

Saurel, D., Orayech, B., Xiao, B., Carriazo, D., Li, X., and Rojo, T. (2018). From charge storage mechanism to performance: a roadmap toward high specific energy sodium-ion batteries through carbon anode optimization. Adv. Energy Mater. *8*, 1703268.

Shen, L., Lv, H., Chen, S., Kopold, P., van Aken, P.A., Wu, X., Maier, J., and Yu, Y. (2017). Peapod-like Li_3VO_4/N-doped carbon nanowires with pseudocapacitive properties as advanced materials for high-energy lithium-ion capacitors. Adv. Mater. *29*, 1700142.

Su, D., and Wang, G. (2013). Single-crystalline bilayered V_2O_5 nanobelts for high-capacity sodium-ion batteries. ACS Nano *7*, 11218–11226.

Thangavel, R., Kaliyappan, K., Kang, K., Sun, X., and Lee, Y.-S. (2016). Going beyond lithium hybrid capacitors: proposing a new high-performing sodium hybrid capacitor system for next-generation hybrid vehicles made with bio-inspired activated carbon. Adv. Energy Mater. *6*, 1502199.

Wang, X., Kajiyama, S., Iinuma, H., Hosono, E., Oro, S., Moriguchi, I., Okubo, M., and Yamada, A. (2015). Pseudocapacitance of MXene nanosheets for high-power sodium-ion hybrid capacitors. Nat. Commun. *6*, 6544.

Wang, H., Zhu, C., Chao, D., Yan, Q., and Fan, H.J. (2017a). Nonaqueous hybrid lithium-ion and sodium-ion capacitors. Adv. Mater. *29*, 1702093.

Wang, P.F., Yao, H.R., Liu, X.Y., Zhang, J.N., Gu, L., Yu, X.Q., Yin, Y.X., and Guo, Y.G. (2017b). Ti-Substituted $NaNi_{0.5}Mn_{0.5-x}Ti_xO_2$ cathodes with reversible O3-P3 phase transition for high-performance sodium-ion batteries. Adv. Mater. *29*, 1700210.

Wei, Q., Liu, J., Feng, W., Sheng, J., Tian, X., He, L., An, Q., and Mai, L. (2015a). Hydrated vanadium pentoxide with superior sodium storage capacity. J. Mater. Chem. A *3*, 8070–8075.

Wei, Q., Tan, S., Liu, X., Yan, M., Wang, F., Li, Q., An, Q., Sun, R., Zhao, K., and Wu, H. (2015b). Novel polygonal vanadium oxide nanoscrolls as stable cathode for lithium storage. Adv. Funct. Mater. *25*, 1773–1779.

Wei, Q., Xiong, F., Tan, S., Huang, L., Lan, E.H., Dunn, B., and Mai, L. (2017a). Porous one-dimensional nanomaterials: design, fabrication and applications in electrochemical energy storage. Adv. Mater. *29*, 1602300.

Wei, T., Yang, G., and Wang, C. (2017b). Iso-oriented $NaTi_2(PO_4)_3$ mesocrystals as anode material for high-energy and long-durability sodium-ion capacitor. ACS Appl. Mater. Interfaces *9*, 31861–31870.

Wei, Q., Wang, Q., Li, Q., An, Q., Zhao, Y., Peng, Z., Jiang, Y., Tan, S., Yan, M., and Mai, L. (2018). Pseudocapacitive layered iron vanadate nanosheets cathode for ultrahigh-rate lithium ion storage. Nano Energy *47*, 294.

Xu, D., Chao, D., Wang, H., Gong, Y., Wang, R., He, B., Hu, X., and Fan, H.J. (2018). Flexible quasi-solid-state sodium-ion capacitors developed using 2D metal-organic-framework array as reactor. Adv. Energy Mater. *8*, 1702769.

Yabuuchi, N., Kubota, K., Dahbi, M., and Komaba, S. (2014). Research development on sodium-ion batteries. Chem. Rev. *114*, 11636–11682.

Yuan, S., Liu, Y.B., Xu, D., Ma, D.L., Wang, S., Yang, X.H., Cao, Z.Y., and Zhang, X.B. (2015). Pure single-crystalline Na1.1V3O7.9 nanobelts as superior cathode materials for rechargeable sodium-ion batteries. Adv. Sci. *2*, 1400018.

Zuo, W., Li, R., Zhou, C., Li, Y., Xia, J., and Liu, J. (2017). Battery-supercapacitor hybrid devices: recent progress and future prospects. Adv. Sci. *4*, 1600539.

ISCI, Volume *6*

Supplemental Information

Sodium Ion Capacitor Using Pseudocapacitive Layered Ferric Vanadate Nanosheets Cathode

Qiulong Wei, Yalong Jiang, Xiaoshi Qian, Liang Zhang, Qidong Li, Shuangshuang Tan, Kangning Zhao, Wei Yang, Qinyou An, Jinghua Guo, and Liqiang Mai

TRANSPARENT METHODS

Synthesis of ferric vanadate nanosheets. Firstly, 6 mmol NH_4VO_3 was dissolved in 200 mL deionized water. Then, 20 mL of 0.1 M $Fe(NO_3)_3$ solution was dropwise added into above solution with stirring and kept at 90 °C for 4 hours. The precipitates with yellow color were formed directly and then turned into brown color after reaction was finished. The brown precipitates were washed by centrifugation with deionized water and pure ethanol for each two times. Finally, the Fe-V-O NSs were obtained after drying in vacuum oven at 80 °C for 12 hours.

Synthesis of hard carbon. The HC was prepared based on previous method with some modifies. (Jian et al., 2016) The sugar (5 g) was fully dissolved in deionized water (40 mL). Then the solution was filled into an autoclave and kept at 180 °C for 5 hours. After drying, the obtained black powder was annealed in a tube furnace at 1100 °C for 5 hours under argon flow. The annealed powder was mixed carbon nanotubes and carbon black at a ratio of 90:5:5 under ball milling at 600 rpm min^{-1} for 4 hours.

Materials Characterization. X-Ray diffraction (XRD) patterns were collected using X-ray diffractometer with a Cu Kα X-ray source. Scanning electron microscopy (SEM) and transmission electron microscopy (TEM) images were collected by using the JEOL-7100F and Titan G2 60-300, respectively. Fourier transform infrared (FT-IR) transmittance spectra were recorded by 60-SXB IR spectrometer. Brunauer-Emmet-Teller (BET) surface area was measured by using Tristar II 3020 instrument. X-ray photoelectron spectroscopy (XPS) was recorded with a VG Multilab 2000. The V and Fe L-edge X-ray absorption spectra (XAS) spectra were measured at the beamline 8.0.1 at the Advanced Light Source, Lawrence Berkeley National Laboratory.

Electrochemical measurements. To fabricate electrodes, the Fe-V-O cathode were prepared by mixing 75% active material, 15% ketjen black and 10% carboxyl methyl cellulose (CMC) binder,

and then coated on Al foil. The 15% of conductive additive is used for providing better electronic conductivity. The HC anode were prepared by mixing 92% of ball milled active material and 8% CMC binder, and then coated on Al foil. After drying in vacuum oven at 120 °C for 6 hours, the electrodes were punched into 10 mm diameter with an active material mass loading of ~2 mg cm^{-2}. Standard CR2025-type coin cells were assembled in an argon-filled glove box. For half-cell test, sodium foil was used as the counter and reference electrode, glass microfiber (Whatman GF/D) as the separator, and 1 M $NaPF_6$ in diethylene glycol dimethyl ether as the electrolyte. For assemble the full HC//Fe-V-O SIC, pre-sodiated HC anode at 0.25 C for 5 cycles were prepared to reduce the irreversibility effect of anode in the initial discharge process and provide the shuttle of Na^+ ions in between the cathode and anode. The mass ratio of HC to Fe-V-O is 1:1, based on the delivered capacity on half-cell testing. Galvanostatic charge/discharge and cyclic voltammetrys were performed by using Bio-Logic VMP3 potentiostats at room temperature. For ex-situ XRD tests the electrode was sealed by tape and for directly texts. The specific energy and average power were calculated according to the $E = \int_{t1}^{t2} IVdt$ and $P = \frac{E}{t}$, where I (A g^{-1}) is the constant current density, V (V) is working voltage, and t is the time (h).

SUPPLEMENTAL FIGURES

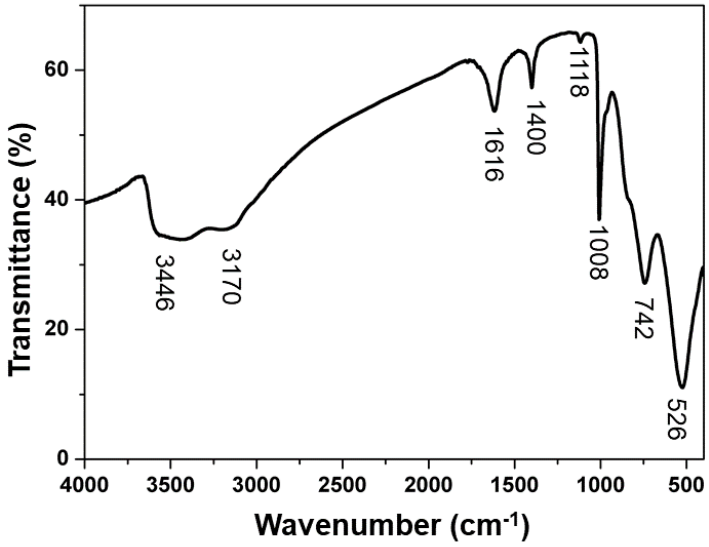

Figure S1. Characterization of Fe-V-O NSs, related to Figure 1.

FT-IR spectrum of Fe-V-O NSs.

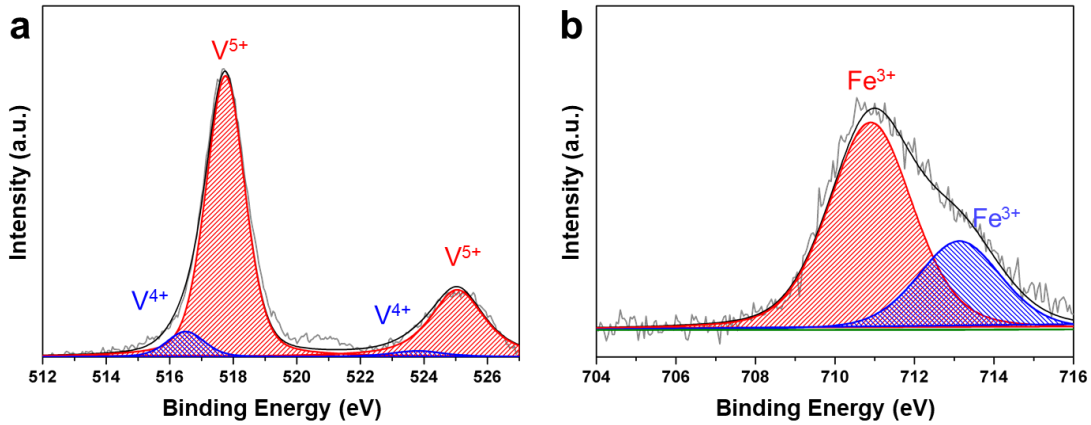

Figure S2. Characterization of Fe-V-O NSs, related to Figure 1.

V 2p (a) and Fe 2p (b) XPS spectra of the layered Fe-V-O NSs.

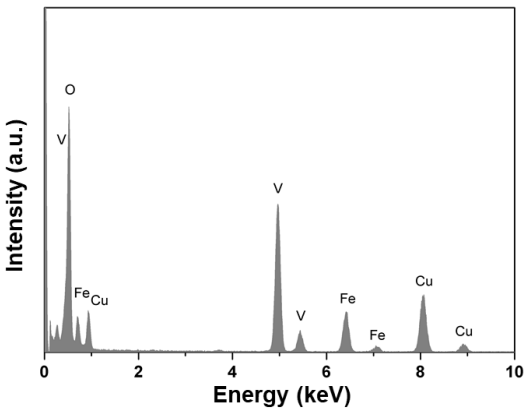

Element	series	Net	[norm. wt.%]	[norm. at.%]
Iron	K-series	9397	17.19	9.4
Vanadium	K-series	30864	51.05	30.4
Oxygen	K-series	19318	31.76	60.2

Figure S3. Characterization of Fe-V-O NSs, related to Figure 1.

EDS spectrum of Fe-V-O NSs. The integrated results indicate that the ratio of V : Fe is 3.23 : 1.

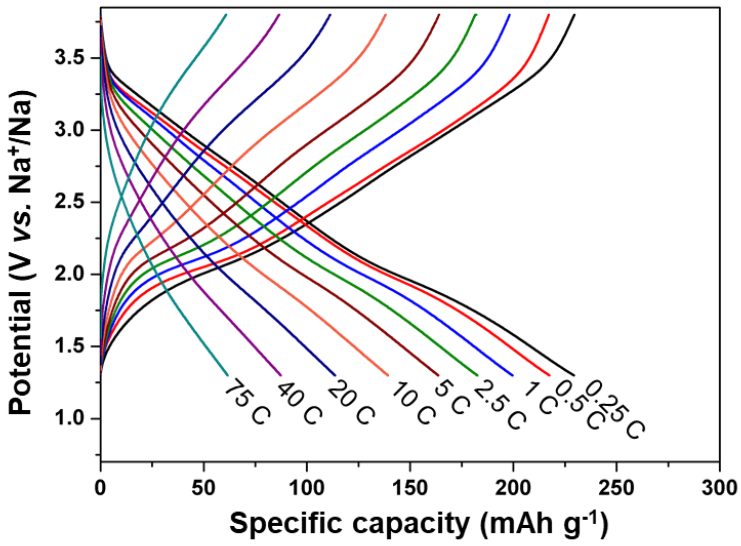

Figure S4. Electrochemical performance of Fe-V-O NSs cathode, related to Figure 2.

The charge-discharge curves of Fe-V-O NSs cathode at various rates from 0.25 to 75 C.

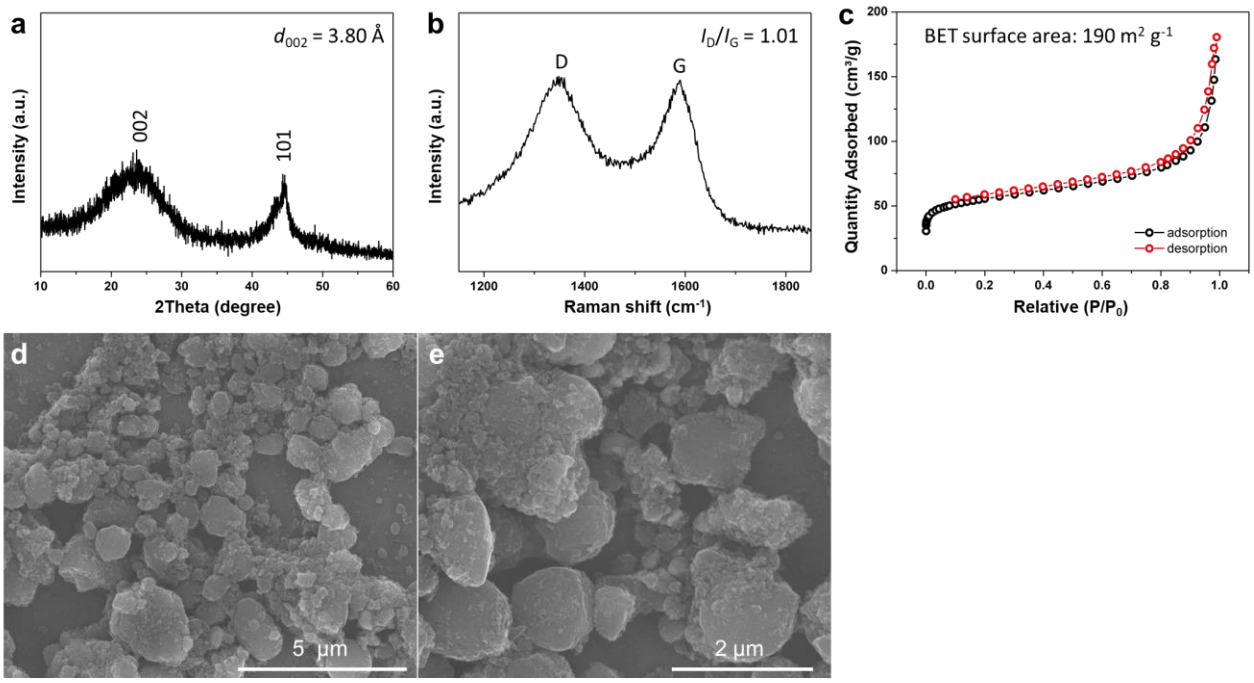

Figure S5. Structure and morphology characterization of hard carbon, related to Figure 4.

XRD pattern (a), Raman spectra (b) and N_2 adsorption-desorption isotherms of hard carbon. (d and e) SEM images of the hard carbon. The d_{002} value is calculated to be 3.80 Å, which is beneficial for large sized Na^+ ion insertion. The I_D/I_G is 1.01, indicating the coexistence of graphite layer and disorder region. The BET surface area of HC is ~190 m^2 g^{-1}. The slop of the N_2 adsorption-desorption isotherms indicates the existence of nanoporous structure.

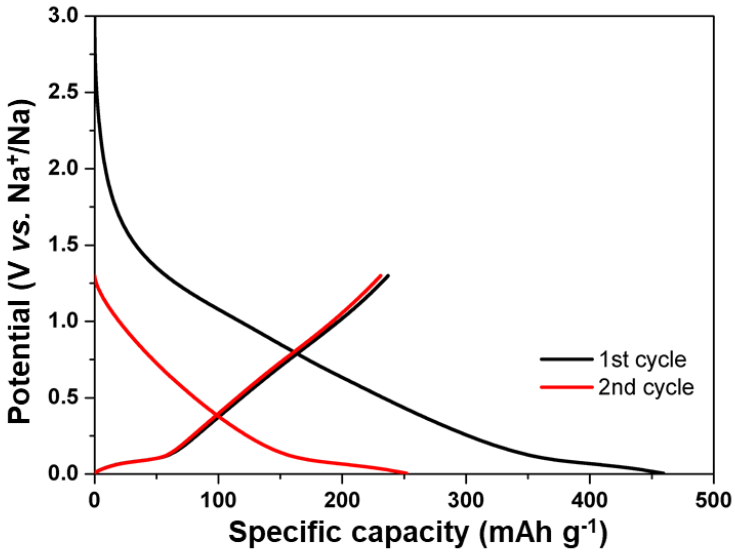

Figure S6. Electrochemical performance of hard carbon anode, related to Figure 4.

The 1st and 2nd charge-discharge curves of HC anode at a rate of 0.25 C. According to the reaction equation: $x\mathrm{C} + \mathrm{Na}^+ + \mathrm{e}^- \leftrightarrow \mathrm{NaC}_x$ and $n = (3.6MC)/F$. The hard carbon delivered a reversible capacity of 240 mAh g^{-1}, corresponding to a sodiated state of $\mathrm{NaC}_{9.7}$. Thus, the weight of hard carbon was increased by ~20% after sodiation.

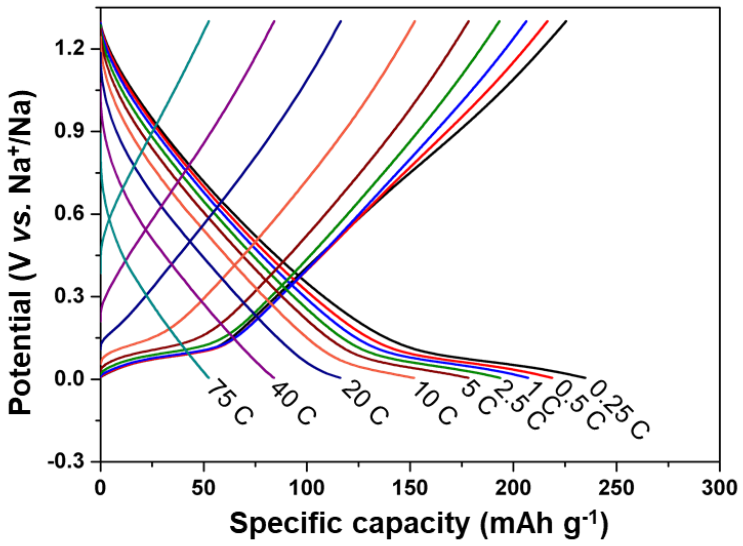

Figure S7. Electrochemical performance of hard carbon anode, related to Figure 4.

The charge-discharge curves of HC anode at various rates from 0.25 to 75 C.

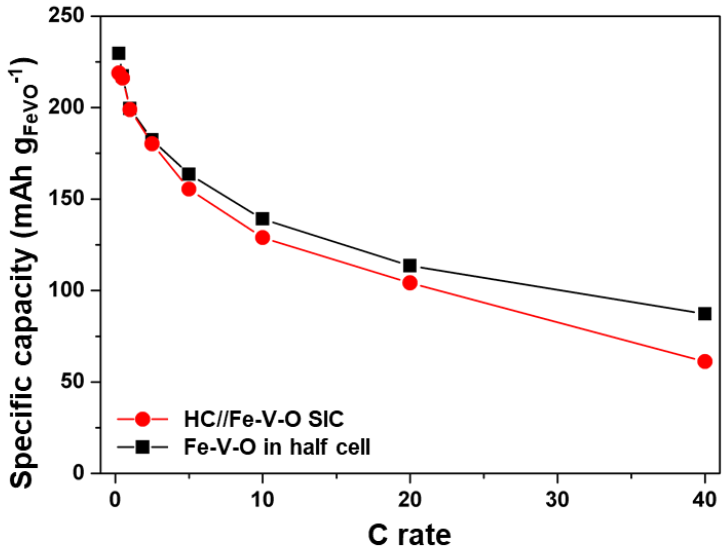

Figure S8. Electrochemical performance of HC//Fe-V-O SIC, related to Figure 5.

The specific capacity of the Fe-V-O tested in full SIC cell and the half cell. For better comparison, the specific capacity shown in the plots is normalized by the mass of Fe-V-O cathode.

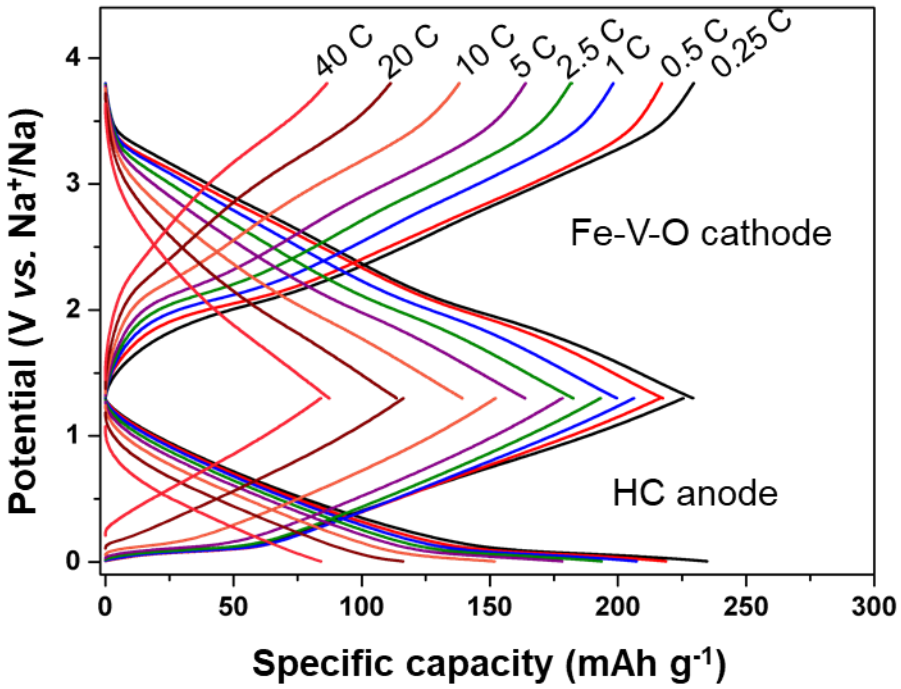

Figure S9. Electrochemical performance of HC//Fe-V-O SIC, related to Figure 5.

Galvanostatic charge−discharge curves of Fe-V-O cathode and HC anode shown at the same C rates. The very similar capacity between cathode and anode at the same C rates indicates well matched kinetics.

SUPPLEMENTAL TABLES

Table S1. The detailed analyses of the XPS results, related to Figure 3.

Peak fit is carried out as the same condition.

Fe-V-O NSs	peak	V^{+3}	V^{+4}	V^{+5}	Fe^{3+}	Fe^{3+}	Fe^{2+}
	location [eV]	515.3	516.5	517.8	710.9	713.1	708.8
Pristine state	area	--	4929	57662	23374	10006	--
	percentage	--	7.9%	92.1%	67.9%	29.1%	--
Discharged state	area	5757	51682	--	2880	6049	4528
	percentage	10.0%	90.0%		21.4%	45.0%	33.6%

SUPPLEMENTAL REFERENCES

Jian, Z., Xing, Z., Bommier, C., Li, Z., and Ji, X. (2016). Hard carbon microspheres: potassium-ion anode versus sodium‐ion anode. Adv. Energy Mater. *6*, 1602898.